Numerical Simulation of a Non-Charring Ablator in High Enthalpy Flows by Means of a Unified Flow-Material Solver

Pierre Schrooyen*
Cenaero, Gosselies, 6041, Belgium

Joffrey Coheur†
von Karman Institute for Fluid Dynamics, Rhode-Saint-Genèse, 1640, Belgium

Alessandro Turchi‡
von Karman Institute for Fluid Dynamics, Rhode-Saint-Genèse, 1640, Belgium

Koen Hillewaert§
Cenaero, Gosselies, 6041, Belgium

Philippe Chatelain¶
Université catholique de Louvain, Louvain-la-Neuve, 1348, Belgium

Thierry E. Magin‖
von Karman Institute for Fluid Dynamics, Rhode-Saint-Genèse, 1640, Belgium

The accurate modeling of the interaction between chemically reactive boundary layers and ablative porous materials is one of the most difficult challenges preventing reliable predictions of the heat flux during atmospheric entries of spacecraft. The unified approach which uses a strong coupled modelization of the flow and the highly porous material has been shown to be necessary in order to capture with high accuracy these interactions in reaction limited regime. In this work, the replication of a Plasmatron experiment with carbon preform material using this methodology has shown that this method allows also to simulate diffusion limited regime giving satisfactory agreements with the experimental data. The thickness of the flow/material interface region has been proved to be a sensitive parameter to guarantee the stability of the simulations and the correct prediction of the quantities of interest.

Latin

A	Arrhenius coefficient
E_a	Arrhenius activation energy, J mol^{-1}
E_tot	Total energy, J kg^{-1}
H_tot	Total enthalpy, J kg^{-1}
h	Enthalpy, J kg^{-1}
h_f^0	Formation enthalpy, J kg^{-1}
k_f	Forward reaction rate

*Research Engineer, Cenaero, Rue des Frères Wright 29, 6041, Gosselies, Belgium; pierre.schrooyen@cenaero.be AIAA Member.

†Ph.D. Student, Aeronautics and Aerospace Department, Chaussée de Waterloo 72, 1640 Rhode-Saint-Genèse, Belgium; joffrey.coheur@vki.ac.be, AIAA Student.

‡Postdoctoral Fellow, Aeronautics and Aerospace Department, Chaussée de Waterloo 72, 1640 Rhode-Saint-Genèse, Belgium; alessandro.turchi@vki.ac.be AIAA Member.

§Research Engineer, Cenaero, Rue des Frères Wright 29, 6041, Gosselies, Belgium; koen.hillewaert@cenaero.be AIAA Member.

¶Assistant Professor, Institute of Mechanics, Material and Civil Engineering, Place du Levant 2, 1348, Louvain-la-Neuve, Belgium; philippe.chatelain@uclouvain.be AIAA Member.

‖Assistant Professor, Aeronautics and Aerospace Department, Chaussée de Waterloo 72, 1640 Rhode-Saint-Genèse, Belgium

l_{abl} Length of ablation, m
$\dot{m}$ Sample mass loss rate, mg s^{-1}
$\dot{m}_{\text{fl}}$ Mass flow rate, g s^{-1}
n Reaction order
P_{el} Electric power supply, W
p Pressure, Pa
$\dot{q}_{\text{cw}}$ Cold wall heat flux, kW m^{-2}
$\mathcal{R}$ Universal gas constant, 8.314 J mol^{-1} K^{-1}
$\dot{s}$ Recession rate, m s^{-1}
S_f Specific surface, m^{-1}
T Temperature, K
$\mathbf{u}$ Velocity vector, m s^{-1}
W Molecular weight, kg mol^{-1}
X Mole fraction
Y Mass fraction

Greek

ξ Emissivity
ϵ Volume fraction
ρ Density, kg m^{-3}
τ Sample exposure time, s
η Tortuosity
ν Stoichiometric coefficient
κ Permeability, m^2
λ Thermal conductivity, W m^{-1} K^{-1}
$\dot{\omega}$ Decomposition rate, kg m^{-3} s^{-1}

Mathematical operators

$\langle\cdot\rangle$ Superficial average operator
$\langle\cdot\rangle_\gamma$ Intrinsic average operator on a single phase γ

Subscript

eff Effective
f Fibers
g Gas phase
s Solid phase
tc Test chamber
w Wall quantity

Superscript

het Heterogeneous reaction
hom Homogeneous reaction

I. Introduction

During the atmospheric entry phase of a spacecraft, a large amount of heat is exchanged between the surrounding gas and the Thermal Protection System (TPS) of the vehicle. For high entry velocity (typically > 11 km/s), ablative materials that can accommodate high heating rates and heat loads through phase change and mass loss are preferred to reusable heat materials.[1] The specific material of interest in this work is low density carbon based composite material. The ablation phenomenon of these kind of materials is a very complex multiphysic problem. The degradation phenomena can be separated mainly in two steps. First, the resin is progressively pyrolyzed, producing pyrolysis gases that percolate through the material and are ejected at the surface in the boundary layer. The pyrolysis process leaves a carbonaceous residue called the char. Then, this charred material is eroded by its interaction with the flow by several physico-chemical phenomena (chemical reactions, sublimation and spallation).[2]

New low density ablative materials have been under investigations and their experimental, as well as their numerical characterization, still need to be improved for a better optimization and design of heat shields. Recently, a large test campaign was performed inside the VKI Plasmatron facility to test those new lightweight ablative materials, using leading-edge measurement techniques and providing a large set of experimental data.[3] On the numerical side, an innovative approach to simulate both the material and the flow in the same domain of computation[a] has been developed the past years[4] and implemented within the multi-dimensional tool Argo, developed at Cenaero. The solver is based on volume averaged Navier-Stokes equations which allows to model the porous ablative material together with the high enthalpy flow. The methodology has been proved to be very important to study low density ablative material since it can capture volume ablation phenomena which can appear with these highly porous material.[5]

This paper focuses on the numerical simulation of high-enthalpy experiments performed inside the VKI Plasmatron facility by means of this unified flow-material approach. In particular, the thermal response of non-charring ablators (carbon preform) is studied in this work. Carbon-preform materials are generally not use directly for TPS but are mainly used as the building block for more complex porous carbon/resin materials. In addition, some carbon preform materials have been proved to have similar properties to charred resin composites.[6] In this paper, a short introduction about the VKI Plasmatron facility and the experimental set-up are presented in Sec. II. We will focus mainly on the test case of a hemispherical shape carbon preform sample that was tested at high pressure and low heat flux. In Sec. III, the model, the

[a]This approach will be referred as unified approach, in contrast to the former decoupled methodologies.

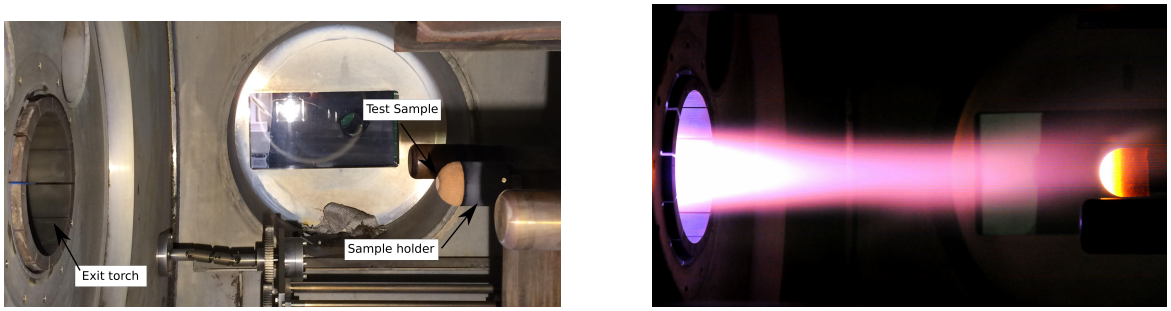
corresponding numerical set-up for this test case are presented and the boundary conditions are discussed. Finally, in Sec. IV, results from the numerical simulations are presented and compared with experimental data.

II. Plasmatron experiments on carbon preform ablation

The *Plasmatron facility* has been extensively used in order to perform research experiments on both reusable and ablative materials for more than a decade. This section mainly focuses on experiments performed on non-charring ablative materials. First, the facility will be presented and the experimental setup is briefly described.

II.A. The VKI Plasmatron facility

The VKI Plasmatron is an Inductively Coupled Plasma (ICP) generator of high power (1.2 MW) which was inaugurated in 1997 and is still the most powerful facility of its kind in the world. Compared to arc-jet plasma wind tunnels, the ICP torch generates a gas with superior purity which is more suitable for gas-surface interaction investigations. Indeed, the use of the ICP torch allows to preserve the heated plasma from pollutants, that are present within combustion-heated facilities and arc-heaters. The experimental chamber of the Plasmatron facility and an ablation test are shown in Fig. 1.



(a) (b)

Figure 1: Pictures of the experimental set-up of the Plasmatron. Left (a), photograph of the test chamber before basalt ablation experiment. Right (b), photograph of an ablation test of carbon-phenolic ablator AQ61 (1 MW/m^2, 15 hPA) by Helber.[3]

At the exit of the torch, the subsonic plasma enters the test chamber, where the test sample is placed. The chamber is usually kept at a pressure between 1200 and 25000 Pa depending on the test conditions. The plasma exits through a diffuser, and is cooled down by a water-cooled heat exchanger. After proper dilution, the products are finally released to the atmosphere through an exhaust. Three parameters fully define the operating conditions of the Plasmatron during TPS testing: the electric power supply P_{el} (kW), the pressure in the test chamber p_{tc} (Pa) and the mass flow rate of fluid $\dot{m}_{\text{fl}}$ (g/s). These parameters are well-defined during a test and typical operating condition ranges are P_{el} between 120 and 300 kW, p_{tc} between 1500 and 20000 Pa and the mass flow rate is often fixed to 16 g/s.[7]

The VKI Plasmatron was initially designed to test lifting body equiped with reusable TPS.[8] The recent work of Helber[3] was the first to investigate the ablation of lightweight TPS in this facility. The recession rate, shape change and gas-surface interaction phenomena are measured and studied.

II.B. Carbon preform ablation test

This section gives more details about the specific test case performed by Helber[3] and investigated numerically in this work. The experimental test conditions of the reference test case and the data collected are given in Table 1. This test case is performed at a pressure of 200 hPa and a heat flux of 1050 kW/m^2, that corresponds roughly to the re-entry conditions of an orbital return.[3] The material tested in this experiment is a non-pyrolyzing Carbon-Bonded Carbon-Fiber (CBCF) material. The experimental material was provided by

Mersen Scotland Holytown Ltd. (CALCARB® CBCF 18-2000).[9] The shape of the sample is a hemispherical sample of radius 25 mm with a total length of 50 mm. This particular hemispherical shape sample is chosen

Test name	gas	p_s	P_{el}	$\dot{q}_{cw}$	τ	T_w	$\dot{s}$	$\dot{m}$	ξ
		hPa	kW	kW/m^2	s	K	μm/s	mg/s	
HS-A2a	air	200	188	1050	91.2	1975	45 ± 1.4	53.2	0.86 ± 0.05

Table 1: Real Plasmatron test conditions for the reference test case (from Helber[3]). Hemispherical (HS) sample, test gas, static pressure p_s, generator power P_{el}, mean cold wall heat flux $\dot{q}_{cw}$, sample exposure time τ, mean surface temperature T_w, recession rate $\dot{s}$, mass loss rate $\dot{m}$ and emissivity of the surface ξ.

because it presents the most stable ablation condition with a fairly constant recession in the radial direction. This choice is also motivated by the relatively low heat flux transferred to the material that results in a lower mass loss, surface recession, wall heat flux and temperature jump between the flow and the material. The experimental data collected during the test campaign which will be used for comparison with the numerical results are described hereafter.

II.B.1. Centerline and volumetric recession

The volume loss of ablated samples was determined using High-Speed Camera (HSC). The camera is used to track the position of the interface of the sample. It appeared that hemispherical shape sample responds with a linear recession rate a few second after the plasma injection. Centerline recession rate obtained from measurement for test case of interest is given in Table 1. A total recession of $\backsim$ 4.45 mm was observed over the whole injection time (90 s).

II.B.2. Mass loss measurements

The mass loss can be estimated either by measuring the mass of the sample before and after the ablation experiments or using the volume loss obtained from HSC. In the last method, axisymetric ablation is assumed and the in-depth mass ablation is neglected. The value given in Table 1 is the mass loss rate obtained from weighting measurement. Discrepancies between the two measurement methods were observed ($\backsim$ 13% for the *HS-A2a* case) because of uncertainties on the material density (180 - 215 kg/m^3, that depends on the manufacturing process), camera resolution, humidity and de-installation process from the sample holder.

II.B.3. Surface radiometry

Infrared radiometers provide information on the thermal behavior of the material samples. Surface temperature is measured using a two-color pyrometer. They measure the radiance at two different wavelength ranges in order to get rid of the emissivity of the surface required in the gray body emission assumption. The emissivity of the test material was also determined using a broadband radiometer (only for the lowest surface temperature tests). An emissivity $\xi = 0.86$ (Tab. 1) was measured for the test case considered here. This material property is required for the numerical simulation as surface cooling due to radiation of the material surface is taken into account. No thermocouples were used in this experiment which would have been interesting to compare with the in-depth temperature field computed numerically.

III. Physical modeling

The methodology is based on the volume averaging theory applied to the reactive Navier-Stokes equations. This continuum description is flexible enough that it can go smoothly from a plain fluid region to a receding porous medium. The material porosity is itself a variable smoothed on the grid during initialization and then computed to track the evolution of the reactive porous medium. The Volume-Averaged Navier-Stokes (VANS) equations for a non-charring reactive porous medium are introduced and implemented inside the numerical solver Argo by Schrooyen et al.[4,5] The integrated numerical tool is based on a multi-physics platform, Argo developed at Cenaero which uses a high order discontinuous Galerkin discretization. A fully implicit solver allows to deal with the stiff source terms introduced in particular by the chemical reactions and

the presence of the porous medium. The thermodynamical and transport properties are obtained through the coupling with a state-of-the-art library Mutation^{++}.[10] In this section, first a summary of the model is given and then the computational domain and boundary conditions to rebuild the Plasmatron experiment are presented. The modeling of the solid and the fluid phase, as well as the set of gas-surface reactions chosen are also discussed.

III.A. Unified model

In order to treat a multi-phases system, the volume averaging approach is used to derive continuum equations.[11] Each phase is described by field quantities which are continuous within this specific medium but discontinuous in the whole volume. Solving the equations for each phase separately requires to account for the microstructure of the porous medium which can be quite complex and computationally expensive. Using volume averaging theory, the equations describing one phase are averaged over a small elementary volume such that the volume averaged quantities are continuous in space. This results in a system of equation valid in the entire domain which is summarized hereafter. More information regarding the derivation of this system of equation can be found in Schrooyen et al.[4] The conservative variables used to describe an ablative material made of carbon preform are the averaged mass density of every species i which needs to be tracked ($\epsilon_\mathrm{g}\langle\rho_i\rangle_\mathrm{g}$), the averaged momentum ($\langle\rho\mathbf{u}\rangle_\mathrm{g}$), the total energy ($\langle\rho E_\mathrm{tot}\rangle$) and the averaged solid density of the fibers ($\langle\rho_\mathrm{s}\rangle$). The intrinsic average of a quantity α on a general phase γ is defined as

$$\langle\alpha\rangle_\gamma \;=\; \frac{1}{dV_\gamma}\int_{dV_\gamma}\alpha\; dv, \tag{1}$$

and has to be distinguished from the superficial average

$$\langle\alpha\rangle \;=\; \epsilon_\mathrm{g}\langle\alpha\rangle_\gamma \;=\; \frac{1}{dV}\int_{dV_\gamma}\alpha\; dv, \tag{2}$$

where dV is the small elementary volume and the porosity (ϵ_g) can be computed as $\epsilon_\mathrm{g} = 1 - \langle\rho_\mathrm{s}\rangle_\mathrm{s}/\langle\rho_\mathrm{s}\rangle$. Using this definition, the VANS system of equations written in vectorial form is

$$\frac{\partial\mathbf{U}}{\partial t} + \nabla\cdot\mathbf{F}^\mathrm{c} = \nabla\cdot\mathbf{F}^\mathrm{d} + \mathbf{S}. \tag{3}$$

with U the conservative variables

$$\mathbf{U} = \begin{pmatrix} \epsilon_\mathrm{g}\langle\rho_i\rangle_\mathrm{g} \\ \langle\rho\mathbf{u}\rangle_\mathrm{g} \\ \langle\rho E_\mathrm{tot}\rangle \\ \langle\rho_\mathrm{s}\rangle \end{pmatrix}. \tag{4}$$

The expression for the convective and diffusive fluxes are

$$\mathbf{F}^\mathrm{c} = \begin{pmatrix} \epsilon_\mathrm{g}\langle\rho_i\rangle_\mathrm{g}\langle\mathbf{u}\rangle_\mathrm{g} \\ \langle\rho\rangle_\mathrm{g}\langle\mathbf{u}\rangle_\mathrm{g}\langle\mathbf{u}\rangle_\mathrm{g} + p \\ \epsilon_\mathrm{g}\langle\rho\rangle_\mathrm{g}\langle\mathbf{u}\rangle_\mathrm{g}\langle H\rangle_\mathrm{g} \\ \mathbf{0} \end{pmatrix}, \text{ and } \mathbf{F}^\mathrm{d} = \begin{pmatrix} -\langle\mathbf{J}_i\rangle \\ \langle\boldsymbol{\tau}\rangle_\mathrm{g} \\ \langle\boldsymbol{\tau}\cdot\mathbf{u}\rangle + \lambda_\mathrm{eff}\nabla\langle T\rangle - \sum_{i=1}^{N_\mathrm{s}} h_i\langle\mathbf{J}_i\rangle \\ \mathbf{0} \end{pmatrix}, \tag{5}$$

where we recall that the averaged mass diffusive flux is

$$\langle\mathbf{J}_i\rangle = -\epsilon_\mathrm{g}\langle\rho_i\rangle_\mathrm{g}\frac{D_{i,\mathrm{m}}}{\eta}\frac{W_i}{W}\nabla X_i + \epsilon_\mathrm{g}\langle\rho_i\rangle_\mathrm{g}\sum_{k=1}^{N_\mathrm{s}}\frac{D_{k,\mathrm{m}}}{\eta}\frac{W_k}{W}\nabla X_k, \tag{6}$$

where $D_{i,\mathrm{m}}$ is the diffusion coefficient of one species in the mixture. Finally, the source term in Eq.(3) is

$$\mathbf{S} = \begin{pmatrix} \langle\dot\omega_i^\mathrm{het}(\langle T\rangle,\langle\rho_i\rangle_\mathrm{g},\langle\rho_\mathrm{s}\rangle)\rangle + \epsilon_\mathrm{g}\dot\omega_i^\mathrm{hom}(\langle T\rangle,\langle\rho_i\rangle_\mathrm{g}) \\ \mathbf{F_{gs}} \\ -\sum_{i=1}^{N_\mathrm{s}+1}\left(\langle\dot\omega_i^\mathrm{het}(\langle T\rangle,\langle\rho_i\rangle_\mathrm{g},\langle\rho_\mathrm{s}\rangle)\rangle + \epsilon_\mathrm{g}\dot\omega_i^\mathrm{hom}(\langle T\rangle,\langle\rho_i\rangle_\mathrm{g})\right)h_{\mathrm{f},i}^0 \\ \langle\dot\omega_i^\mathrm{het}(\langle T\rangle,\langle\rho_i\rangle_\mathrm{g},\langle\rho_\mathrm{s}\rangle)\rangle \end{pmatrix}, \tag{7}$$

where $\mathbf{F_{gs}}$ is the momentum exchange term between the two phases. In this work, the closure of this term only includes the first order drag force predicted by Darcy. The homogeneous production term for each species is given by

$$\dot{\omega}_i^{\text{hom}} = W_i \sum_{k=1}^{N_r} (\nu''_{ik} - \nu'_{ik}) \left(k_{f,k} \prod_{j=1}^{N_s} \tilde{\rho}_j^{\nu'_{j,k}} - k_{b,k} \prod_{j=1}^{N_s} \tilde{\rho}_j^{\nu''_{j,k}} \right). \tag{8}$$

In Eq. (8), $\tilde{\rho}$ is the molar density, $k_{f,k}$ and $k_{b,k}$ are the forward and backward reaction rates, $\nu_{i,k}$ are the stoichiometric coefficients and the exponents $'$ and $''$ represent respectively the reactants and products. The averaged heterogeneous production rate for reacting species is modeled as

$$\langle \dot{\omega}_i^{\text{het}} \rangle = \frac{1}{dV} \oint_{\partial\Omega_g} -k_f \langle \rho_A \rangle_{\text{gs}} \, dS. \tag{9}$$

It is trivial to observe that if ϵ_g tends to one, additional source terms disappear and this system of equations reduces to the classical Navier-Stokes equations for multi-species flows.

III.B. Numerical setup

This section presents the computational domain and the boundary conditions used. In addition, the parameters used to close the model presented in Section III.A are discussed.

III.B.1. Computational domain and boundary conditions

Since we are mainly interested to study the flow/material interaction, the computational domain do not consider the torch and the entire Plasmatron chamber shown in Fig. 1. The geometry of the domain considered with the boundary conditions is presented in Fig. 2. The inlet boundary is 13 cm away from the sample surface, a preliminary run using an internal 1D stagnation line code[12] showed that this is sufficient to capture accurately the flow field. The length of the holder behind the material is assumed to be 25 mm. It worth to emphasize that there are no boundaries between the fluid medium and the solid material. The refinement of the mesh in the flow/material interface is performed to capture the phenomena in the vicinity of the interface. Indeed, strong gradients should be captured in this region (temperature, velocity, concentration of species, change of solid density) requiring a high resolution. The use of coarser meshes has shown that the recession of the interface can not be captured accurately and a maximum of ≈ 40 μm for the cell size is required.

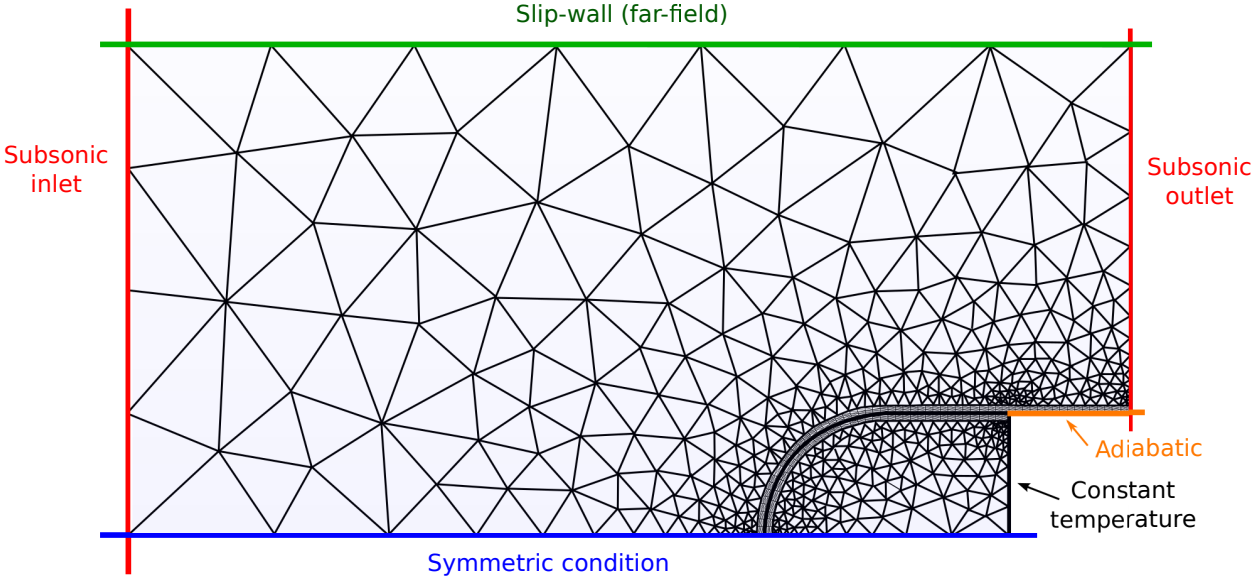


Figure 2: Computational domain of the Plasmatron experiment.

In this computation, the unstructured mesh is composed of 2644 triangular elements. The total number of elements is relatively low, but the number of degrees of freedom becomes relatively high when considering a large number of species in the fluid mixture. A second order Lagrangian polynomial interpolation is used inside each elements reaching a total number of nodes of 158640.

The conditions imposed at the boundaries of the computational domain represented in Fig. 2 are summarized in Table 2. The freestream conditions are extracted from an established procedure at VKI. First the subsonic freestream plasma flow coming from the ICP torch is characterized by a magnetohydrodynamic solver.[13] Then, the boundary layer edge conditions obtained from the magnetohydrodynamic solver are used as input for a boundary layer code. The code then rebuild the conditions at the boundary layer edge of a non-reactive, catalytic boundary layer by iterating on the outer edge temperature to wall heat-flux measurements. The freestream value obtained from the 1D simulation is then imposed on the whole subsonic inlet. Species mass fractions at the inlet are obtained from the equilibrium composition of a mixture of air composed of 5 species (N, O, NO, N_2, O_2). The pressure at the outlet is the one corresponding to the experimental set-up (Table 1) and is equal to 200 hPa in this case. An adiabatic boundary conditions is assumed for the wall of the holder.

Table 2: Summary of the boundary conditions for the Plasmatron test case. Inlet velocity U_{in}, inlet temperature T_{in}, outlet pressure p_{out}. The species mass fractions Y_{in} are expressed in the following order: $\text{N}, \text{O}, \text{NO}, \text{N}_2, \text{O}_2, \text{CO}$.

Subsonic inlet	$U_{\text{in}} = 37$ ms^{-1}, $T_{\text{in}} = 6088$ K
	$Y_{\text{in}} = \{0.27, 0.23, 0.0036, 0.49, 5e\text{-}5, 0\}$
Subsonic outlet	$p_{\text{out}} = 20000$ Pa

III.B.2. Solid phase

The material tested is the non-pyrolyzing Carbon-Bonded Carbon-Fiber (CBCF) material already presented in Sec. II.B. The following assumptions are made for the numerical simulation. First, the fibers are made of pure carbon. No preferential direction in the fibers is modeled, that would results in non-scalar material properties. The initial radius of the fibers is equal to 5 μm. Secondly, we assume that the material has a nominal bulk initial density of 180 kg/m^3 with an initial porosity of 90%. The thermal conductivity is provided by the manufacturer and a constant value of 0.5 W/m-K is used. In addition, permeability and tortuosity must be provided to close the models. For the permeability, an initial value of $1.45e^{-10}$ m^2 is chosen and is assumed to evolve with porosity according to the semi-empirical model of Carman-Kozeny.[14] Concerning the tortuosity of the porous medium, an initial value of 1.1 is adopted[15] and it evolves linearly between freestream tortuosity ($\eta = 1$) and its initial value.

III.B.3. Fluid phase

The fluid is considered to be a mixture of 6 chemical species: 5 for the inflow air (N_2, O_2, N, O, NO) and one product of oxidation (CO). These are assumed to be thermally perfect gas. Finite rate chemistry for the homogeneous reactions are used and the reaction rate are taken from Park.[16] In the mechanism used, the products of the heterogeneous reaction CO is assumed to be frozen and does not react with the surrounding gas. Thermo and transport properties are computed using the Mutation^{++} library[10] with the NASA-9 polynomial coefficient module for the thermodynamic properties and the Chapman-Enskog method for the transport properties.

III.B.4. Surface reaction rates

Chemical reactions between the fluid and the solid (heterogeneous reactions) need to be modeled as well. Those are mainly responsible of the surface ablation of the material and in this case, we assume that

	Reacting species	
	O	O_2
A	3.22	5.73
$E_a/\mathcal{R}$	0	9.65e3
n	0.5	0.5

Table 3: Arrhenius coefficient for oxidations reactions of carbon fibers.

only chemical reactions induce the recession of the surface, i.e. no sublimation and no mechanical erosion (spallation) are considered. The following oxidation reactions are considered within this work

$$O + C(s) \rightarrow CO \tag{10}$$

$$O_2 + 2C(s) \rightarrow 2CO \tag{11}$$

for which reverse reactions does not need to be considered as the equilibrium constant is very small.[16] The presence of CN was also observed experimentally by means of Optical Emission Spectroscopy (OES)[3] however reactions with atomic nitrogen are not taking into account in the present work. The forward reactions rates for the two previous reactions are obtained from Arrhenius type law of the form

$$k_f^{i,C(s)} = AT^n \exp\left(\frac{-E_a}{\mathcal{R}T}\right) \tag{12}$$

where i denotes the limiting species and the Arrhenius coefficients are taken from Park[16] and given in Table 3. It is also worth to note that no wall catalysis is considered at the surface of the material. To close Eq. (9), the evolution of specific surface S_f with the ablation of the fibers still need to be modeled. In this case, we are assuming that the fibers are cylindrical and that they recess uniformly and in the radial direction as proposed by Lachaud.[17]

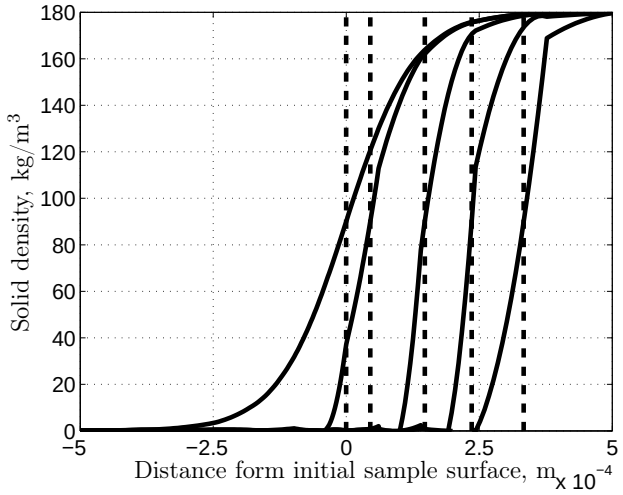
IV. Analysis of the results

Results of the numerical simulations are presented and compared with the experimental data in this section. Only few seconds (8 s) were simulated because it has been proved to be enough to reach the quasi-steady state for recession observed on hemispherical-shape samples and it allows to reduce drastically the computational cost. Indeed, to capture efficiently the interface, the mesh in the receding zone should be sufficiently fine. Therefore, reducing the simulation time allows also to have a shorter refined zone.

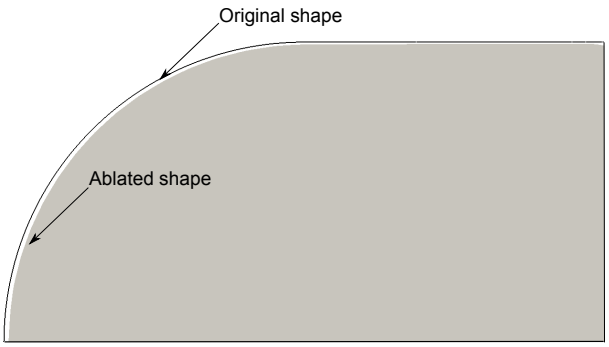
IV.A. Solid density and mass

Since the porosity of the material progressively decreases from its constant value to zero in the pure fluid region, the gas-solid interface is not sharp anymore but rather a region with a certain thickness. Nonetheless, a definition of the interface position is needed to characterize the evolution of the shape and compute the recession velocity. As proposed in Schrooyen et al.,[5] we choose here to define the interface position as the region where the porosity is half the maximum value in the transition region. The evolution of the solid density profile with time and the corresponding interface position can be observed in Fig. 3a. The interface region which is smoothed at initialization is progressively decreased with time which shows that these conditions corresponds to a surface ablation regime (diffusion limited). Indeed, the solid density in-depth does not change and the oxidation phenomenon is concentrated at the surface of the sample. This will be further discussed in Section IV.E. It can also be observed that since the interface becomes sharper, the capture of this interface becomes more challenging. The final 2D axisymetric shape of the ablated sample after 8 s can be observed in Fig. 3b. The experimental volumetric recession[3] shows a radial recession with a shape very similar to the one computed numerically.

The stagnation point recession can also be computed based on the previous definition of the interface. Fig. 4a shows the recession with time, which becomes, as observed experimentally, linear quickly after the

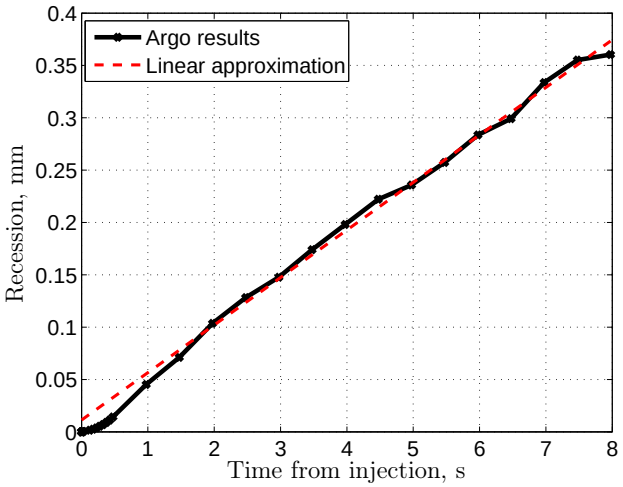


(a) Solid density along the stagnation line

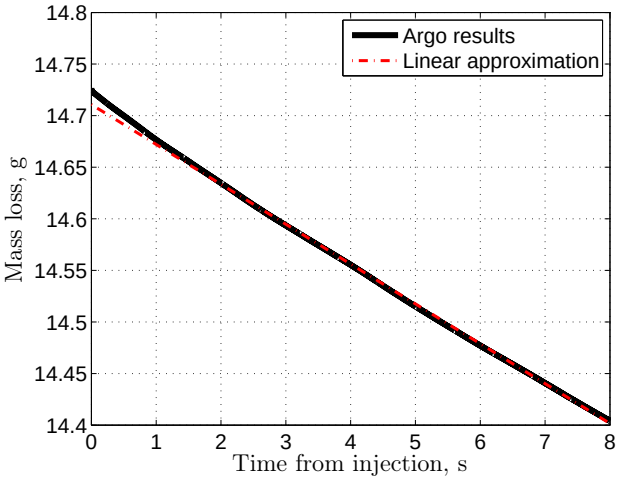


(b) Shape of the ablated sample

Figure 3: Computed volumetric recession of the carbon preform sample using Argo. (a) Solid density along the stagnation line for several time steps. From left to right, the time is 0, 1, 3, 5, and 7 s respectively. (b) Shape of the ablated sample after 8 s of simulation.



(a) Stagnation point recession



(b) Mass loss

Figure 4: Recession of the surface at the stagnation line (a) and mass loss (b) during 8 s of carbon preform exposition to Plasmatron environement.

beginning of the ablation process. The small oscillations in the recession can be explained by the post-processing to compute the exact interface position. The recession rate is computed to be 45.4 μm/s which is very close to the experimental velocity measured(45 ± 1.4 μm/s). The total mass loss can be observed in Fig. 4b. It can be observed that quickly the mass loss becomes linear and a quasi-steady ablation regime is achieved. The mass loss rate computed in the steady regime (after 1 s) is 38.6 mg/s which leads to a 27% difference with respect to the experimental value. Since the recession velocity computed is very similar to the one obtained experimentally and the ablation phenomenon appears mostly close to the surface, a possible explanation for this discrepancy is that it comes from the uncertainties regarding the solid density of sample ($180 - 215$ kg/m^3).[3]

IV.B. Surface temperature

The heat exchange between the incoming high enthalpy flow and the porous material will progressively lead to an increase of the temperature field inside the material. This temperature increase at the surface of the material is enhanced by exothermic reactions at the wall (such as atomic nitrogen recombination and oxidation reaction of the fibers). The stagnation point temperature is shown in Fig. 5 and compared with experimental data.

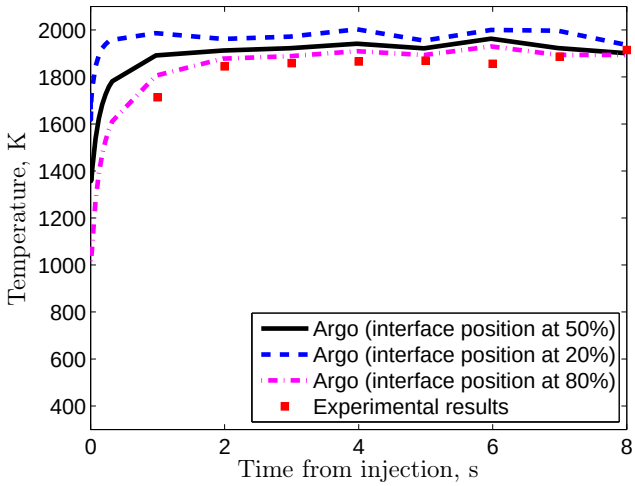
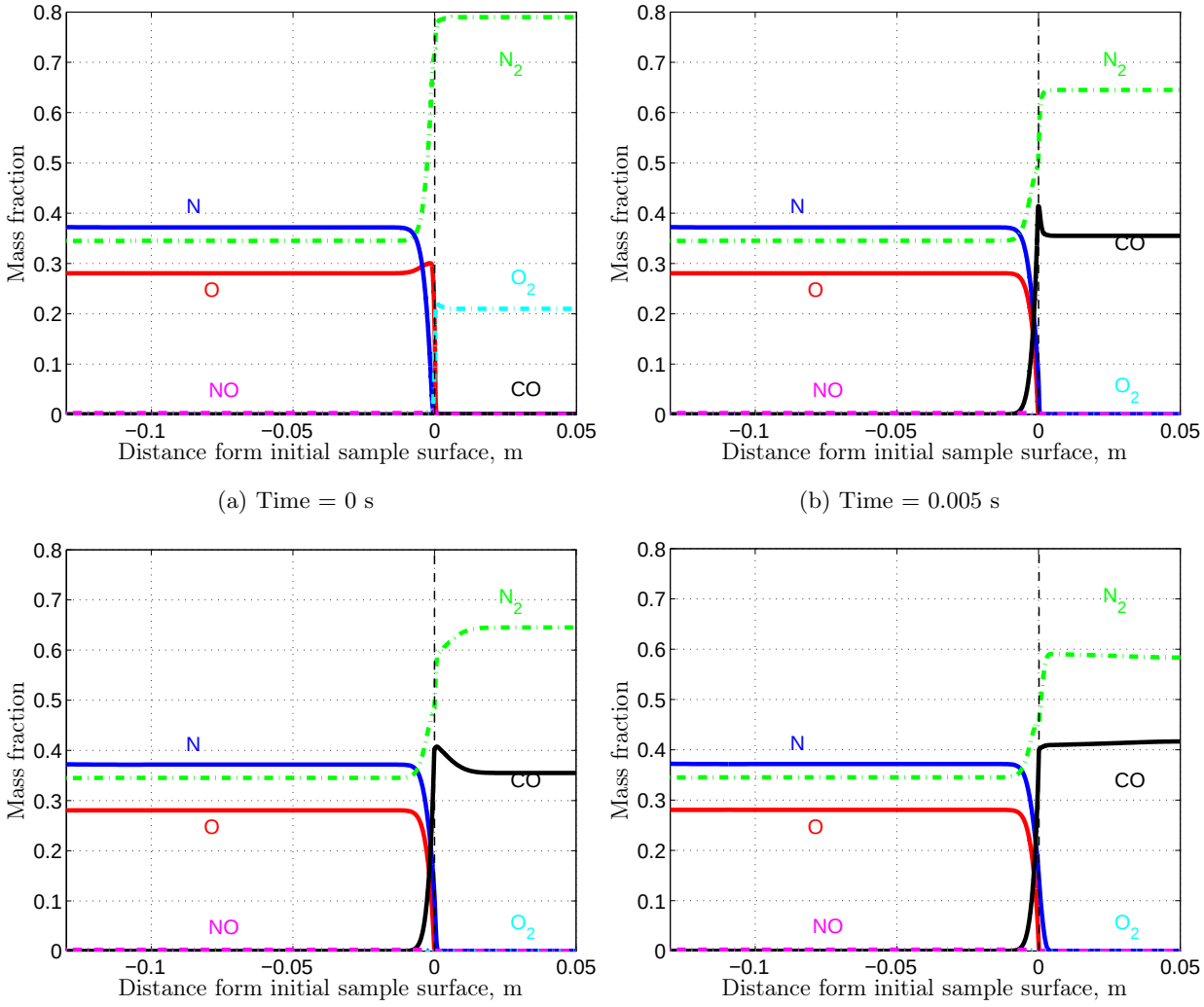


Figure 5: Stagnation point temperature of the carbon preform material.

The experimental value and the numerical results using the previous definition of the interface are close but slightly overestimate the temperature at the stagnation point. In Fig. 5, two other definitions to post-process the interface position are used to evaluate the influence of this definition. We are considering a definition for the interface at 20% of its maximum value and at 80% in order to have bounds of the temperature value at the stagnation point inside the interface transition region. This define a temperature range for the stagnation point temperature. Since the temperature gradient close to the surface is high, a slight error in the interface position might lead to a different temperature computed at the surface. This post-processing effect results in the oscillations observed for each definition of the interface. In this surface ablation regime where the solid density variation becomes sharper, this phenomenon becomes more important.

IV.C. Species mass fraction

Since one mass conservation equation per species is solved at each time step (see Eq. (3)), this allows to track the production of species and, in particular, the one produced by heterogeneous chemical reactions. The mass fraction at several times are shown in Fig. 6. At the initialization, no carbonaceous species are present in the flow field or the material. Once the heterogeneous reaction starts, a peak of CO is observed directly (see Fig. 6b) at the surface of the sample that arises from the reaction of carbon with the oxygen species (both O_2 and O). The production of CO at high temperature comes mainly from the reaction with atomic oxygen, that is also diffusing inside the material on a distance l_{abl} also called the ablation depth. At lower temperature, the CO comes mainly from the reaction of the fibers with molecular oxygen. Using the rate given in Table 3, the O_2 reacts immediately with the carbon of the fibers which explains the CO produced inside the porous material. Then, the CO produced at the surface of the material is progressively convected and diffused inside the porous medium to reach after a while a constant mass fraction value (see Fig. 6d) with a steady state production rate at the surface.



(a) Time = 0 s

(b) Time = 0.005 s

(c) Time = 0.2 s

(d) Time = 3 s

Figure 6: Species mass fractions along stagnation line.

IV.D. Static pressure

The result for the static pressure along the stagnation line is shown in Fig. 7 and is extracted at $t = 3$ s when the steady state ablation is reached. A peak of 20009 Pa is observed at the surface of the sample. A simple estimation of the pressure at the wall can be obtained using Bernoulli's principle on the stagnation line

$$p_{\mathrm{w}} = p_{\mathrm{s}} + \frac{\rho u^2}{2} \tag{13}$$

where p_{s} and p_{w} are respectively the static pressure and the pressure at the wall, ρ is the fluid density and u is the freestream velocity. The density of the gas at the freestream temperature (6088 K) is 0.007677 kg/m^3 and the velocity being equal to 37 m/s, a value of 20005 Pa is obtained. This simple estimation does not consider compressible effects but these are negligible at low Mach number. However, a correction for viscous effect that arises at low Reynolds number (Barker effect), typically below 100, can be used for the estimation of the stagnation pressure

$$p_{\mathrm{w}} = \frac{1}{2}\rho u^2 K_H + p_{\mathrm{s}} \tag{14}$$

where K_H is the Homann's correction factor[18] given by

$$K_H = 1 + \frac{6}{Re + 0.455\sqrt{Re}}. \tag{15}$$

The Reynolds number is based on the radius of the sample and the freestream conditions, leading to $Re = 42.3$. Bernoulli's formula with the Homann's correction gives a static pressure at the wall of 20006 Pa. Both approximation give close results because of the relatively large radius of the sample, compared to small pitot probes on which the effect can lead to error larger than 10%.[19] The numerical value obtained and these approximations are very close (less than 0.1% of difference). Note that the theoretical approximation does not account for the blowing at the surface of the material which can also explain the higher pressure at the stagnation point computed with ARGO.

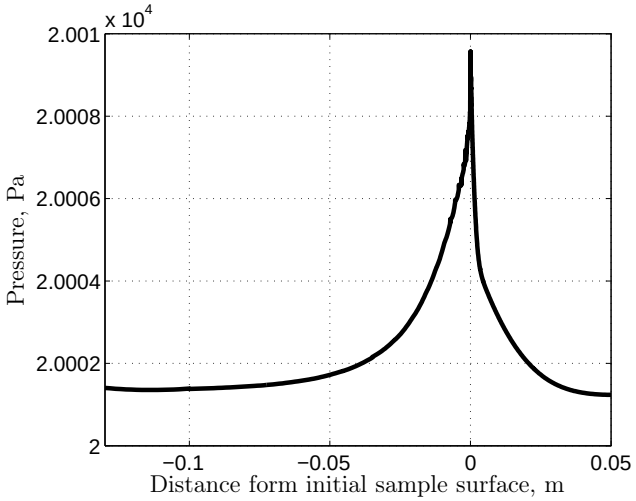


Figure 7: Pressure along the stagnation line at time 3[s].

The methodology used also allows to capture the pressure field inside the porous sample. This already gives an idea on how the flow will behave in the vicinity of the interface. Finally, note that the absolute variation of pressure is really small, one can observe small oscillations in the vicinity of the interface which indicates that the resolution is not sufficient to capture accurately these small variations.

IV.E. Length of ablation

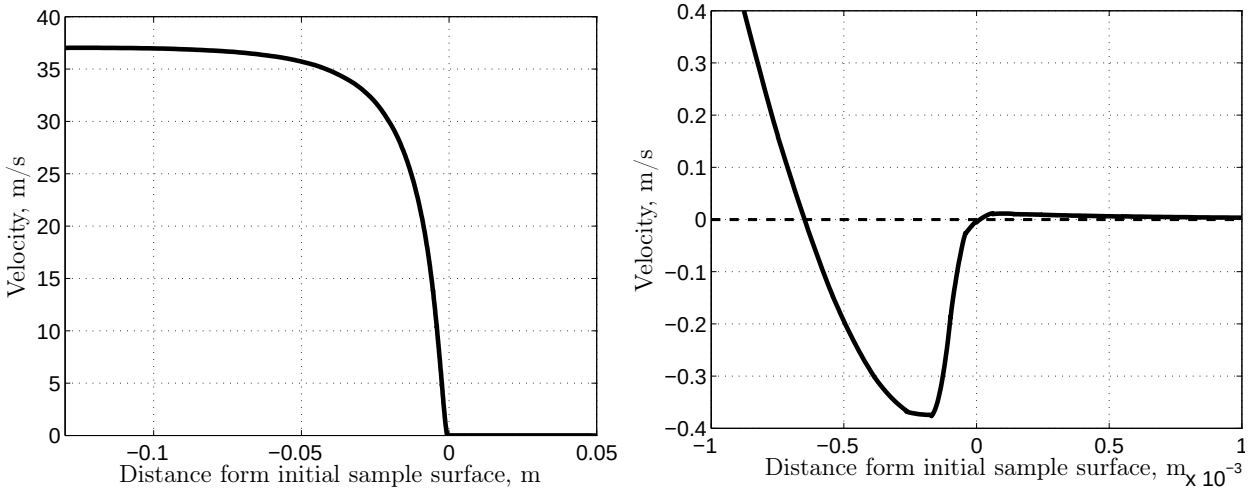
Most of the state-of-the-art thermal response codes[20–22] are assuming that ablation is only a surface phenomenon. This assumption was widely used in the past for the design of heat shields using dense TPS.[20] The hypothesis of a mere surface ablation is not accurate enough for low density material with high porosity.[15] The ablation phenomenon for lightweight materials was shown to occur also below the surface of the sample.[23] This in-depth ablation is also referred as volume ablation. The Thiele number reflects the competition between surface and volume ablation

$$Th = \frac{L}{\sqrt{D_{\text{eff}}/S_f k_f}} = \frac{L}{l_{\text{abl}}},$$

where D_{eff} is the effective diffusion coefficient, L is a characteristic length and l_{abl} is the length of ablation driven by oxygen diffusion and fiber reactivity. The oxygen penetration depth l_{abl} can be directly obtained from the numerical simulations by observing the depth at which atomic oxygen decreases towards zero. This length is computed starting from the interface position which is defined using the criterion explained in Sec. IV.B and is found to be ≈ 125 μm. The corresponding Thiele number based on the radius of the sample is $Th = 200$ while the experiments shows a $Th = 360$. A value of $Th > 50$ suggests a diffusion-limited ablation process. In this regime, the oxygen is consumed directly at the surface and does not have time to penetrate inside the porous medium (i.e. surface ablation is observed). The regime observed in the experiment and in the numerical replication is the same but the value of Thiele number seems quite different. Once again, the definition of the interface position and the thickness of the transition region should be taken into account for a fair comparison with experimental data.

IV.F. Velocity fields

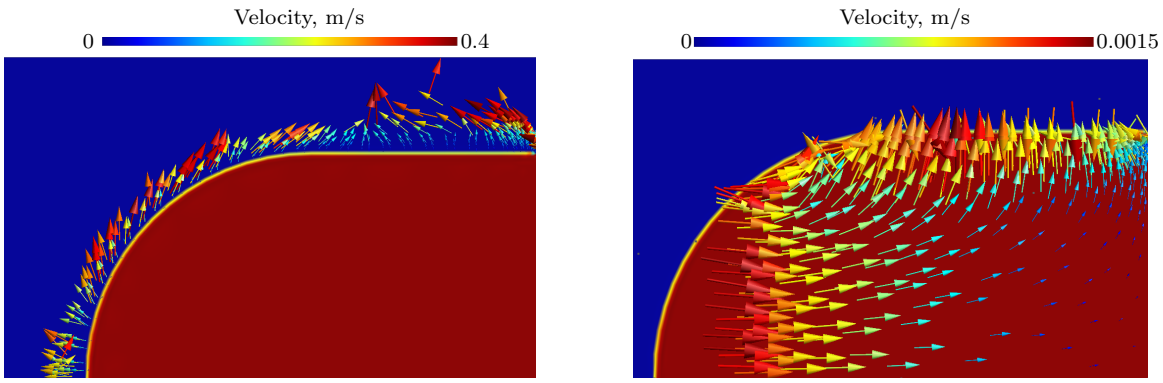
Fig. 8 shows the axial velocity along the stagnation line. First, it can be observed that the velocity starts to decrease noticeably at 5 cm upstream of the sample and goes to a value close to zero at the surface of the sample. Close to the outer part of the sample surface, a backward flow can be observed due to the blowing of carbonaceous products from the ablation process (see Fig. 8b). The CO produced from the heterogeneous reaction between the incoming oxygen and the fibers is injected in the boundary layer. In addition, inside the porous material, a flow of low velocity (Stokes flow) is observed, ranging from 0 to 0.01 m/s on the edges of the material. The 2D velocity vector field inside the porous medium is shown in Fig. 9 and is in agreement with the discussion of Sec. IV.D. It also shows the 2D effects of such configuration in this Plasmatron experiment.



(a) Axial velocity

(b) Closed view

Figure 8: Stagnation line velocity field at t=0.2 s after injection of the sample in the high enthalpy flow.



(a) (b)

Figure 9: Velocity vector field at the edge of the material (a) and inside the porous medium (b).

V. Conclusion

The unified approach developed in Schrooyen et al.[5] has been successfully used to simulate an experiment conducted in the Plasmatron facility. This methodology aims at capturing accurately the interactions between the flow and the ablated geometry by strongly coupling the simulation of flow field and thermal material response. Within this work, this unified approach developed mainly to study volume ablation for low density porous material has shown good agreements with experimental data even in a surface ablation regime. The Argo code correctly captures the recession at the surface of the material giving a rate and a shape close to the experimental results. The mass loss computed numerically underestimates the experimental value but the large uncertainty on the solid density is considered to be the reason of this discrepancy. A sensitivity analysis based on this parameter is proposed to verify this assumption. In addition, the increase of temperature of the material surface was shown to be sensitive to the definition of the surface position arising from the smoothing of the interface. Furthermore, several runs on coarse meshes have shown the need to refine the interface region to correctly capture the recession and evolution of the ablated sample geometry. The perspectives of this work are to reproduce other test cases within different ablation regimes to see the limit of this methodology. Finally, a comparison with other classical approaches is also envisioned to determine the regime in which such approach is really needed.

VI. Acknowledgment

The authors would like to thank B. Helber for the data provided on the experiment and used as comparison. J. Coheur is also gratefull to the von Karman Institute for the nine months fellowship provided during the Research Master program during which this study was performed.

References

[1]Duffa, G., *Ablative thermal protection systems modeling*, American Institute of Aeronautics and Astronautics, Inc., Reston,Virginia, 2013.

[2]Lachaud, J., Magin, T. E., Cozmuta, I., and Mansour, N. N., "A Short Review of Ablative-Material Response Models and Simulation Tools," *7th European Symposium on Aerothermodynamics*, edited by L. Ouwehand, SP-692, ESTEC-ESA, Brugge, Belgium, May 2011.

[3]Helber, B., *Material Response Characterization of Low-Density Ablators in Atmospheric Entry Plasmas*, Ph.D. thesis, Vrije Universiteit Brussel & von Karman Institute for Fluid Dynamics, Belgium, 2016.

[4]Schrooyen, P., *Numerical Simulation of Aerothermal Flows Through Ablative Thermal Protection Systems*, Ph.D. thesis, Université Catholique de Louvain & von Karman Institute for Fluid Dynamics, Belgium, Belgium, 2015.

[5]Schrooyen, P., Hillewaert, K., Magin, T., and Châtelain, P., "Fully Implicit Discontinuous Galerkin Solver to Study Surface and Volume Ablation Competition in Atmospheric Entry Flows," *International Journal of Heat and Mass Transfer*, Vol. 103, 2016, pp. 108–124.

[6]Stackpoole, M., Sepka, S., Cozmuta, I., and Kontinos, D., "Post-Flight Evaluation of Stardus Sample Return Capsule Forebody Heatshield Material," *Journal of Thermophysics and Heat Transfer*, Vol. 24, No. 4, 2010, pp. 694–707.

[7]Bottin, B., Carbonaro, M., Paris, S., Vanderhaegen, V., Novelli, A., and Vennemann, D., "VKI 1.2 MW Plasmatron Facility for the Thermal Testing of TPS Materials," *3rd European Workshop on Thermal Protection Systems*, The Netherlands, March 1998.

[8]Bottin, B., Chazot, O., Carbonaro, M., Van Der Haegen, V., and Paris, S., "The VKI Plasmatron Characteristics and Performance," Tech. rep., von Karman Inst. for Fluid Dynamics, Rhode-Saint-Genèse (Belgium), 2000.

[9]Mersen, "Calcarb rigid carbon thermal insulation," Technical guide HT 29 GB 0121, Mersen, 2011.

[10]Scoggins, J. and Magin, T. E., "Development of Mutation++: Multicomponent thermodynamic and transport property library for ionized plasmas written in C++," *11th AIAA/ASME Joint Thermophysics and Heat Transfer Conference*, AIAA Paper 2014-1966, Atlanta, GA, 16-20 June 2014.

[11]Whitaker, S., *The Method of Volume Averaging*, Vol. 13 of *Theory and Applications of Transport in Porous Media*, Springer Netherlands, 1st ed., 1999.

[12]Turchi, A., Helber, B., Munafò, and E., M. T., "Development and Testing of an Ablation Model Based on Plasma Wind Tunnel Experiments," *11th AIAA/ASME Joint Thermophysics and Heat Transfer Conference*, AIAA Paper 2014-1966, Atlanta, GA, 16-20 June 2014.

[13]Magin, T., *A Model for Inductive Plasma Wind Tunnels*, Ph.D. thesis, Université Libre de Bruxelles & Von Karman Institute for Fluid Dynamics, Belgium, 2004.

[14]Dullien, F., *Porous media: fluid transport and pore structure*, Academic Press, San Diego, 1991.

[15]Lachaud, J., Cozmuta, I., and Mansour, N. N., "Multiscale approach to ablation modeling of phenolic impregnated carbon ablators," *Journal of Spacecraft and Rockets*, Vol. 47, No. 6, 2010, pp. 910–921.

[16]Park, C., Jaffe, R. L., and Partridge, H., "Chemical-kinetic parameters of hyperbolic earth entry," *Journal of Thermophysics and Heat Transfer*, Vol. 15, No. 1, 2001, pp. 76–90.

[17]Lachaud, J., Mansour, N., Ceballos, A., Pejakovic, D., Zhang, L., and Marschall, J., "Validation of a volume-averaged fiber-scale model for the oxidation of a carbon-fiber preform," *42nd AIAA Thermophysics Conference*, No. AIAA 2011-3640, American Institute of Aeronautics and Astronautics, Honolulu, HA, 27-30 June 2011.

[18]Homann, F., "The effect of high viscosity on the flow around a cylinder and around a sphere," Technical memorandum 1334, NACA, 1952, Translation of "Der Einfluss grosser Zähigkeit bei der Strömung um den Zylinder und um die Kugel", ZAMM, vol. 16, no. 3, June 1936.

[19]Magin, T. E., "Cooled Pitot probe in air plasma jet," *I3MS Seminar Series*, Aachen, Germany, 13 July 2015.

[20]Kendall, R. M., Barlett, E. P., Rindal, R. A., and Moyer, C. B., "An Analysis of the Coupled Chemically Reacting Boundary Layer and Charring Ablator: Part I." CR-1060, NASA, 1968.

[21]Chen, Y.-K., Milos, F., and Gökcen, T., "Validation of a three-dimensional ablation and thermal response code," *10th AIAA/ASME Joint Thermophysics and Heat Transfer Conference*, No. AIAA 2010-4645, American Institute of Aeronautics and Astronautics, 28-30 June 2010.

[22]Dec, J., Braun, R., and Laub, B., "Ablative Thermal Response Analysis Using the Finite Element Method," *Journal of thermophysics and heat transfer*, Vol. 26, No. 2, 2012, pp. 201–212.

[23]Panerai, F., Martin, A., Mansour, N. N., Sepka, S. A., and Lachaud, J., "Flow-tube oxidation experiments of the carbon preform of a phenolic-impregnated carbon ablator," *Journal of Thermophysics and Heat Transfer*, Vol. 28, No. 2, 2014, pp. 181–190.